


Cite this: *Nanoscale*, 2021, **13**, 9641

Macroscopic and microscopic picture of negative capacitance operation in ferroelectric capacitors†

David Esseni  and Riccardo Fontanini 

The negative capacitance (NC) operation of ferroelectric materials has been originally proposed based on a homogeneous Landau theory, leading to a simple NC stabilization condition expressed in terms of macroscopic quantities. A multi-domain theory, however, has pointed out the importance of microscopic parameters, such as the domain wall energy coupling constant, and it helped explain the somewhat contradicting experiments for ferroelectric capacitors with or without a metal interlayer. In this work we use comprehensive numerical simulations and simplified equations to correlate the macroscopic features of the NC operation to the underlying microscopic picture. We show that, while the domain wall coupling constant plays a critical role in a quasi static operation, the transient NC operation is less sensitive to this parameter. In particular, ferroelectric capacitors with a very small coupling constant can still display a robust transient NC behavior, closely tracking the 'S'-shaped polarization *versus* field curve and with negligible hysteresis. Our results have been developed in the framework of a systematic comparison between simulations and experiments, and they provide both a better understanding of the NC operation and a sound basis for the design of future NC based devices.

Received 25th September 2020,

Accepted 4th May 2021

DOI: 10.1039/d0nr06886a

rsc.li/nanoscale

1 Introduction

The negative capacitance operation of ferroelectric capacitors is an interesting and partly elusive topic from a material science perspective,^{1–3} and it is a promising option for the design of nanoscale transistors.^{4–6} In this latter respect, several studies have experimentally reported NC operation in MOS transistors and discussed the potential benefits up to industrial level CMOS circuits,^{7,8} and other contributions have addressed different design aspects related to NC transistors.^{9–18}

A condition for the NC operation of a Metal–Ferroelectric–Insulator–Metal (MFIM) capacitor relying only on macroscopic material and device parameters is very useful from a device design standpoint. For a homogenous polarization (or, equivalently, for a single domain picture) the NC stabilisation is entirely governed by the depolarization energy and the stabilisation condition has been derived as^{19,20}

$$\frac{1}{(C_D + C_F)} > 2|\alpha|t_F \quad (1)$$

where α is the anisotropy constant of the P term in the ferroelectric dynamic equations (see eqn (2) below), and C_D , C_F are defined as $C_D = \epsilon_0 \epsilon_D / t_D$, $C_F = \epsilon_0 \epsilon_F / t_F$ (with t_D , ϵ_D being the thick-

ness and relative permittivity of the dielectric, and t_F , ϵ_F being the thickness and background permittivity of the ferroelectric). When a multi-domain picture is considered, however, it has been argued that the NC stabilisation is influenced by the coupling constant k of the domain wall energy,¹⁹ and a k dependent condition for the NC stabilisation has been recently derived in ref. 20 and 21.

From an experimental standpoint, a direct NC observation was first claimed for a single layer $\text{Pb}(\text{Zr}_{0.2}\text{Ti}_{0.8})\text{O}_3$ (PZT) thin film connected in series to an external resistance,²² where the decreasing ferroelectric voltage for increasing ferroelectric charge was proposed as the evidence of an NC operation. While alternative interpretations have been proposed for the above experiments,^{23,24} then an experimental evidence of the NC behavior was reported in ferroelectric–dielectric heterostructures exhibiting an overall capacitance larger than the capacitance of the constituent layers,^{25,26} as well as in ferroelectric superlattices.²⁷ The discovery of ferroelectricity in hafnium oxides opened exciting perspectives for applications in CMOS technologies,^{28,29} and several reports have appeared about a steep slope operation in ferroelectric based transistors.^{30–32} The steep slope behavior in nanoscale transistors is frequently accompanied by hysteresis, and it has been interpreted by some authors as a feature caused by the dynamics of the domain nucleation process.^{33–35} More recently, however, a measurement of the negative capacitance branch of a thin $\text{Hf}_{0.5}\text{Zr}_{0.5}\text{O}_2$ in MFIM capacitors has been reported in ref. 36 and 37, and a spatial mapping of the

DPIA, University of Udine, Via delle Scienze 206, 33100 Udine, Italy.

E-mail: david.esseni@uniud.it

†Electronic supplementary information (ESI) available. See DOI: 10.1039/D0NR06886A

steady-state negative capacitance in SrTiO₃/PbTiO₃ superlattices has been published in ref. 38.

In this paper we employ a comprehensive model of an MFIM capacitor based on the multi-domain Landau, Ginzburg, Devonshire (LGD) theory and analyze the operation of Hf_{0.5}Zr_{0.5}O₂ based MFIM structures in the framework of a comparison between our simulations and the experiments in ref. 37. Our results show that a quasi static NC operation requires the fulfillment of the homogeneous NC stability condition, that is critically influenced by the domain wall coupling constant k . For the Hf_{0.5}Zr_{0.5}O₂ based MFIM structures, in particular, this requires unrealistically large k values. Nevertheless MFIM systems not meeting the homogeneous NC stability can still display an evident transient NC behavior, which tracks the 'S'-shaped polarization *versus* field curve with a negligible hysteresis. In this scenario our simulations can reproduce well the experiments in ref. 37 even for negligible values of the coupling constant k .

2 Ferroelectric dynamic equations

Let us now consider the MFIM system sketched in Fig. 1 and consisting of n_D domains. Our starting point is given by the multi-domain LGD equations for the ferroelectric dynamics in a MFIM capacitor presented in ref. 20, where it is assumed that the spontaneous polarisation P lies along the z direction, and the depolarisation energy is expressed by duly accounting for the three-dimensional nature of the electrostatics in the device. The dynamic equation for domain i (with $i = 1, 2, \dots, n_D$) reads

$$t_F \rho \frac{dP_i}{dt} = - (2\alpha_i P_i + 4\beta_i P_i^3 + 6\gamma_i P_i^5) t_F - \frac{t_F k}{d w} \sum_n (P_i - P_n) - \frac{1}{2} \sum_{j=1}^{n_D} \left(\frac{1}{C_{ij}} + \frac{1}{C_{ji}} \right) P_j + \frac{C_D}{C_0} V_T \quad (2)$$

where α_i , β_i and γ_i are the domain dependent ferroelectric anisotropy constants, C_0 is $(C_D + C_F)$, k is the coupling constant

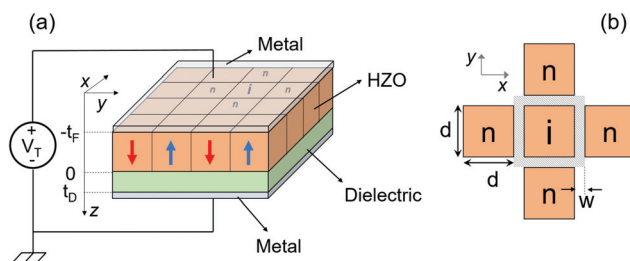


Fig. 1 Ferroelectric capacitors and related symbols. (a) Sketch of a MFIM capacitor, where t_F and t_D are the ferroelectric and dielectric thicknesses. A positive ferroelectric polarization points towards the dielectric (red arrow). (b) Zoom on the ferroelectric domain wall regions, where d is the side of the square domain and w is the width of the domain-wall region, which are used to calculate the domain wall energy.²⁰ V_T is the external bias, while $V_D(\vec{r})$ and $V_F(\vec{r})$ are the voltage drop respectively across the dielectric and ferroelectric, depending on the position $(\vec{r}) = (x, y)$ in the (x, y) plane.

governing the domain wall energy, while capacitances C_{ij} are defined in eqn (S5) of ESI S1 and obey the sum rules in eqn (S6).[†] As it can be seen in Fig. 1, d and w in eqn (2) denote respectively the domain side and the width of the domain-wall region.²⁰ The resistivity ρ sets the time scale of the ferroelectric dynamics, that can be approximately defined as $t_\rho = \rho/(2|\langle\alpha\rangle|)$, where $\langle\alpha\rangle$ is the mean value of the α_i .

Eqn (2) form a set of n_D coupled dynamic equations that we solved numerically to determine the trajectory of each P_i during the transient enforced by an external stimulus $V_T(t)$. As it can be seen eqn (2) provide a microscopic information on individual domains, whereas in electrical experiments it is usually possible to access only macroscopic quantities, such as the average polarization $P_{AV} = \left(\sum_{j=1}^{n_D} P_j \right) / n_D$ and the corresponding average electric fields across the ferroelectric and the dielectric.

In a strongly correlated domain dynamics the polarization of individual domains has only a modest deviation from the P_{AV} , but along more general dynamic trajectories such deviations can be large. In this respect, we here introduce the deviation $\Delta P_i = (P_i - P_{AV})$ of P_i from the average polarization P_{AV} , and then define the second and third order P_i moments as

$$\mu_{2P} = \left[\frac{1}{n_D} \sum_{i=1}^{n_D} (P_i - P_{AV})^2 \right]^{1/2} \quad (3)$$

$$\mu_{3P} = \left[\frac{1}{n_D} \sum_{i=1}^{n_D} (P_i - P_{AV})^3 \right]^{1/3}$$

The moments μ_{2P} and μ_{3P} will be useful in the analysis of the NC behavior developed below.

Based on eqn (2), a stable NC operation consisting in the polarization P_i of all domains being zero at zero external voltage V_T has been studied in ref. 20, and the stability condition has been derived as

$$\sigma_{\min} \left[\frac{t_F k}{d w} \mathbf{L} + \mathbf{C}_{\text{dep}} \right] > 2|\alpha| t_F \quad (4)$$

where $C_{\text{dep}}(i, j)$ is defined component-wise as $C_{\text{dep}}(i, j) = (1/2) [1/C_{ij} + 1/C_{ji}]$, \mathbf{L} is the Laplacian matrix,[‡] and $\sigma_{\min}[\mathbf{M}]$ denotes the smallest eigenvalue of the matrix \mathbf{M} .

In this work we will refer to eqn (4) as the homogeneous NC stability condition. For a system fulfilling eqn (4) it is guaranteed a hysteresis-free behavior for a quasi static operation, namely for an external stimulus that is slow enough to drive the system practically through a sequence of steady states. However an MFIM system that does not meet eqn (4) can still display a theoretically and technologically relevant transient NC behavior, that will be further discussed in section 3.4.

[†] \mathbf{L} is defined component-wise as $L(i, j) = (1 \text{ if domain } j \text{ is a neighbour of domain } i \text{ and } L(i, j) = 0 \text{ otherwise (see Fig. 1), and } L(i, i) = -\sum_{j \neq i} L(i, j))$.

3 Macroscopic and microscopic features of the NC operation

In this section we discuss the link between the macroscopic features of the MFIM operation (*e.g.* the hysteresis and the slope of the NC branches), and the microscopic picture given by, for example, the trajectories of the individual domains and μ_{2P} . This will be developed in the framework of a comparison between our simulations and the transient NC measurements in ref. 36 and 37, namely for MFIM capacitors consisting of $\text{Hf}_{0.5}\text{Zr}_{0.5}\text{O}_2$ and either a Ta_2O_5 or an Al_2O_3 dielectric. For the $\text{Hf}_{0.5}\text{Zr}_{0.5}\text{O}_2$ - Ta_2O_5 system we have $t_F = 11.6$ nm, $t_D = 13.5$ nm, while for the $\text{Hf}_{0.5}\text{Zr}_{0.5}\text{O}_2$ - Al_2O_3 system t_F is 7.7 nm and t_D is 4 nm; all other material parameters are reported in Table 1. If not otherwise stated, simulations were carried out for an MFIM capacitor consisting of $n_D = 20 \times 20$ domains,[§] and for a domain size $d = 5$ nm. The width of the domain-wall region was set to $w = 0.5$ nm (see Fig. 1(b)), which is an appropriate value for several ferroelectric materials.¹⁹ For all the MFIM systems studied in this work, the capacitances C_{ij} were evaluated numerically as explained in ref. 20.

While the above α , β figures in Table 1 are the nominal values of the anisotropic parameters for $\text{Hf}_{0.5}\text{Zr}_{0.5}\text{O}_2$ (that set also the nominal values for the coercive field, E_C , and remanent polarization, P_r), in our analysis we also accounted for a domain to domain random variation of α_i , β_i constants (still keeping $\gamma = 0$). In order to have a clear physical picture of the statistical dispersion in the system, our starting point is a normal distribution of E_C , with σ_{EC} denoting the ratio between the standard deviation and the mean value of E_C . For any realization of an MFIM capacitor, a set of n_D instances for $E_{C,i}$ is generated and the corresponding α_i and β_i values are calculated by using the analytical expressions $\alpha_i = -3\sqrt{3}E_{C,i}/(4P_r)$, $\beta_i = 3\sqrt{3}E_{C,i}/(8P_r^3)$ that hold for $\gamma = 0$; no dispersion of the remnant polarisation P_r was considered in the calculations. If not otherwise stated, the simulation results were obtained for a value $\sigma_{EC} = 10\%$ of the ratio between the standard deviation and the mean value of E_C .

3.1 Quasi static operation and influence of the domain wall coupling constant

In this paper we let $Q = P + \epsilon_F \epsilon_0 E_F$ denote the total charge per unit area in the MFIM capacitor, while the total ferroelectric polarisation is $P_T = P + (\epsilon_F - 1)\epsilon_0 E_F$.⁴⁰ Throughout this section simulations correspond to a very slow waveform for the external bias V_T corresponding to transition times of about $500t_F$, which ensure a quasi static behavior of the MFIM system. For each simulation set, μ_{2P} was evaluated numerically according to the definition in eqn (3).

Fig. 2 shows the charge *versus* the ferroelectric field, E_F , characteristic for either a $\text{Hf}_{0.5}\text{Zr}_{0.5}\text{O}_2$ - Ta_2O_5 MFIM system (in Fig. 2(a)–(c)), or a $\text{Hf}_{0.5}\text{Zr}_{0.5}\text{O}_2$ - Al_2O_3 system (in Fig. 2(d)), for a

Table 1 Material parameters used in simulations for the $\text{Hf}_{0.5}\text{Zr}_{0.5}\text{O}_2$ - Ta_2O_5 and the $\text{Hf}_{0.5}\text{Zr}_{0.5}\text{O}_2$ - Al_2O_3 MFIM system, and for the BaTiO_3 based MFIM system

	HZO- Ta_2O_5 ^{20,37}	HZO- Al_2O_3 ^{20,37}	BaTiO_3 ^{3,39}
α [m F^{-1}]	-4.6×10^8	-9.45×10^8	-2.77×10^7
β [$\text{m}^5 \text{C}^{-2} \text{F}^{-1}$]	9.8×10^9	2.25×10^9	-6.381×10^8
γ [$\text{m}^9 \text{C}^{-4} \text{F}^{-1}$]	0	0	7.89×10^9
ϵ_F	33	33	417
ϵ_D	23.5	8	208

domain size $d = 5$ nm and for different values of the domain wall constant k . It has been shown in ref. 20 that for the $\text{Hf}_{0.5}\text{Zr}_{0.5}\text{O}_2$ - Ta_2O_5 system the homogeneous NC stability condition in eqn (4) requires a k value larger than approximately $7 \times 10^{-10} [\text{m}^3 \text{F}^{-1}]$ (see also Fig. 6(a)).

Fig. 2(a) reports the simulated charge *versus* E_F curves for $k = 2 \times 10^{-9} \text{ m}^3 \text{F}^{-1}$ showing that, for such a k value fully satisfying eqn (4), the charge to field relation tracks the negative capacitance branch and is hysteresis free, moreover simulations agree well with the experiments in ref. 37.

Fig. 2(b) and (c) show that for smaller k values, instead, the polarization *versus* field trajectories become hysteretic, and the onset of the hysteresis is correlated to a large increase of the moment μ_{2P} , namely to a large domain to domain variations of the polarization. In particular, μ_{2P} is maximum approximately where the average polarization P_{AV} goes through zero. Fig. 2(c) also shows on the right vertical axis the second order moment

$$\text{of the ferroelectric field } \mu_{2E_F} = \sqrt{(1/n_D) \sum_{i=1}^{n_D} (E_{F,i} - E_{F,AV})^2},$$

where $E_{F,i}$ and $E_{F,AV}$ denote, respectively, the z component of the field in the ferroelectric domain i and the domain averaged field. As expected the large domain to domain variations of P_i result in similarly large variations of the field across the ferroelectric and the dielectric layer.

Fig. 2(d) shows that the analysis of the $\text{Hf}_{0.5}\text{Zr}_{0.5}\text{O}_2$ - Al_2O_3 MFIM essentially confirms the main results observed in Fig. 2(a)–(c) for the $\text{Hf}_{0.5}\text{Zr}_{0.5}\text{O}_2$ - Ta_2O_5 system. In particular, in quasi static conditions and for a coupling constant $k = 2 \times 10^{-9} \text{ m}^3 \text{F}^{-1}$, the $\text{Hf}_{0.5}\text{Zr}_{0.5}\text{O}_2$ - Al_2O_3 system exhibits a non hysteretic charge to field relation with a negligible μ_{2P} , and simulations agree well with the experiments in ref. 37. For $k = 2 \times 10^{-11} \text{ m}^3 \text{F}^{-1}$, instead, a hysteresis loop opens in the simulated charge *versus* field curve, accompanied by large μ_{2P} values.

Here it should be remarked that the large μ_{2P} values at small k observed in Fig. 2 correspond to a spontaneous behavior of the MFIM capacitor in quasi static conditions. In fact Fig. 3 shows that, for $k = 2 \times 10^{-11} \text{ m}^3 \text{F}^{-1}$, the Q *versus* $E_{F,AV}$ trajectories of the system and the μ_{2P} values are hardly affected by the standard deviation σ_{EC} of the domain to domain variations of the ferroelectric coercive field. Even for a σ_{EC} as small as 0.5% a large μ_{2P} is observed during the ferroelectric switching process for the simulation conditions of Fig. 2.

Fig. 4 compares the charge *versus* ferroelectric field curves for $t_D = 13.5$ nm and $t_D = 2$ nm in quasi static conditions. For the thinnest dielectric the condition $(C_D + C_F) < 1/(2|\alpha|t_F)$ is

[§] We have verified that results are insensitive to the number of domains for n_D larger than approximately 100.

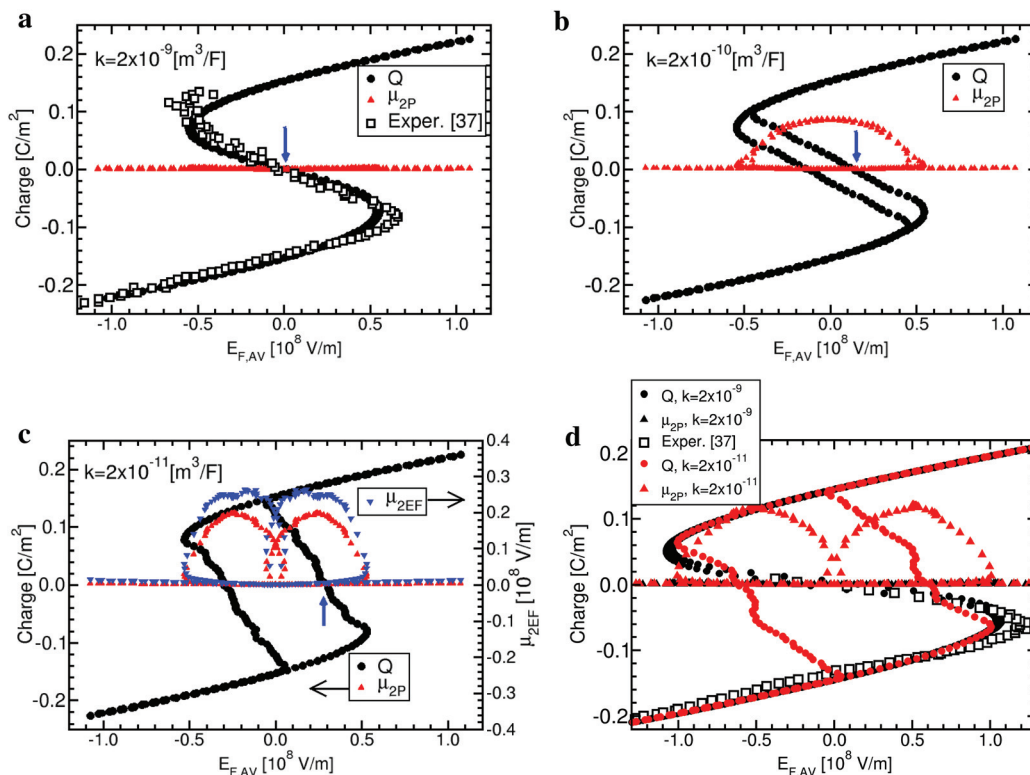


Fig. 2 Influence of the domain wall energy coupling constant on the quasi static NC behavior. Simulations and experiments for: (a)–(c) a $\text{Hf}_{0.5}\text{Zr}_{0.5}\text{O}_2\text{--Ta}_2\text{O}_5$ MFIM system; (d) a $\text{Hf}_{0.5}\text{Zr}_{0.5}\text{O}_2\text{--Al}_2\text{O}_3$ system; the material and physical parameters are given at the beginning of section 3. The size of the domains is $d = 5$ nm (see Fig. 1). (a) Charge, Q , and second order P_i moment, μ_{2P} , versus average ferroelectric field for a domain wall constant $k = 2 \times 10^{-9} \text{ m}^3 \text{ F}^{-1}$. Open squares report the measurements from ref. 37. (b) Q and μ_{2P} versus average ferroelectric field as in (a), but for $k = 2 \times 10^{-10} \text{ m}^3 \text{ F}^{-1}$; (c) same as in (b) but for $k = 2 \times 10^{-11} \text{ m}^3 \text{ F}^{-1}$. The second order E_F moment, $\mu_{2E_F} = \sqrt{(1/n_D) \sum_{i=1}^{n_D} (E_{F,i} - E_{F,AV})^2}$, is also reported on the right y axis. (d) Same as in (a) but for the $\text{Hf}_{0.5}\text{Zr}_{0.5}\text{O}_2\text{--Al}_2\text{O}_3$ system and for a domain wall constant of either $k = 2 \times 10^{-9} \text{ m}^3 \text{ F}^{-1}$ (black) or $k = 2 \times 10^{-11} \text{ m}^3 \text{ F}^{-1}$ (red). Open squares report experiments from ref. 37.

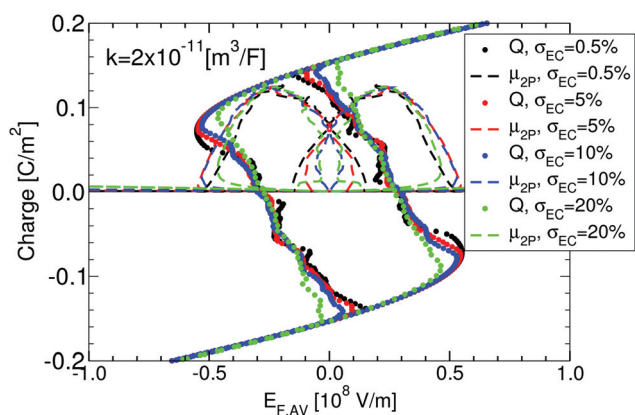


Fig. 3 Influence of the domain to domain variations of the ferroelectric parameters. Charge, Q , and second order P_i moment, μ_{2P} , versus average ferroelectric field for a domain wall coupling constant $k = 2 \times 10^{-11} \text{ m}^3 \text{ F}^{-1}$ and for different values of the normalized standard deviation, σ_{EC} , of the ferroelectric coercive field. All other parameters are as in Fig. 2. More details about the inclusion in simulations of domain to domain variations can be found in the second paragraph of section 3.

not fulfilled and Fig. 4(a) shows that, as expected, the system with the thin oxide is hysteretic even for a relatively large $k = 2 \times 10^{-9} \text{ m}^3 \text{ F}^{-1}$. However the second order P_i moment, μ_{2P} , is relatively small, and for $t_D = 2$ nm the slope ($dQ/dE_{F,AV}$) in the NC branches is fairly close to the slope of the $t_D = 13.5$ nm system, which instead satisfies the homogeneous NC stability condition. Fig. 4(b) reports the same comparison but for $k = 2 \times 10^{-11} \text{ m}^3 \text{ F}^{-1}$, corresponding to a hysteretic behavior for both $t_D = 13.5$ nm and $t_D = 2$ nm. In this case we observe large μ_{2P} values, and the charge versus $E_{F,AV}$ curve is similar for the two very different dielectric thicknesses.

The simulation results in Fig. 2 and 4 show that the onset of a hysteretic behavior in quasi static conditions is accompanied by a significant increase in the magnitude of the negative slope ($dQ/dE_{F,AV}$) along the negative capacitance branches. The magnitude of the slope enlarges for increasing μ_{2P} values and thus for an increasing amplitude of the hysteresis. In ESI S1† we show that the ($dQ/dE_{F,AV}$) in the NC branches can be approximately expressed as

$$\frac{dQ}{dE_{F,AV}} \simeq \frac{1}{2(\alpha + 6\beta\mu_{2P}^2)} + \epsilon_F \epsilon_0. \quad (5)$$

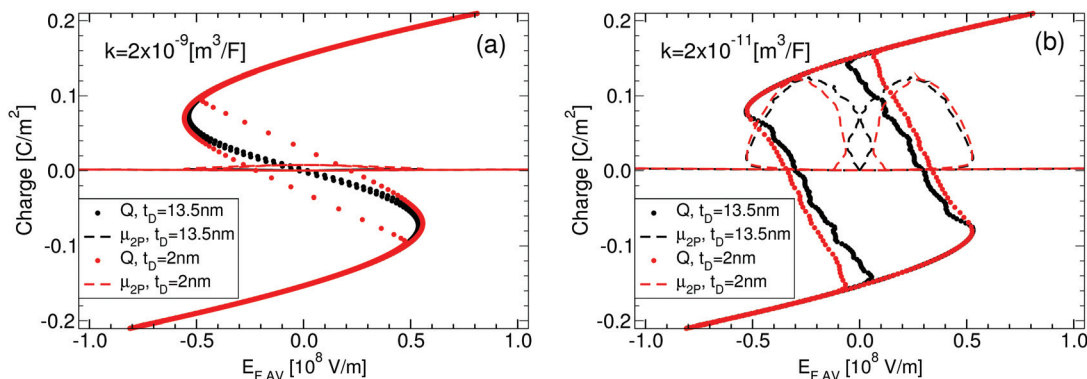


Fig. 4 Charge versus ferroelectric field curves for different dielectric thicknesses. Charge, Q , and second order P_i moment, μ_{2P} , versus average ferroelectric field for either $t_D = 13.5$ nm (black, same results as in Fig. 2) or $t_D = 2.0$ nm (red). All other parameters are as in Fig. 2. (a) Domain wall coupling constant $k = 2 \times 10^{-9} \text{ m}^3 \text{ F}^{-1}$; (b) Domain wall coupling constant $k = 2 \times 10^{-11} \text{ m}^3 \text{ F}^{-1}$.

Eqn (5) shows that, because α is negative and $(dQ/dE_{F,AV})$ is also negative in the region of interest, then the magnitude of $(dQ/dE_{F,AV})$ increases for increasing μ_{2P} , which is the trend observed in Fig. 2 and 4.

3.2 Quasi static operation and free energy analysis

In order to gain a physical insight about the large influence of the domain wall coupling constant on the quasi static characteristics illustrated in Fig. 2–4, we analyzed the total free energy, U_T , the depolarization energy, U_{dep} , and the domain wall energy U_W of the $\text{Hf}_{0.5}\text{Zr}_{0.5}\text{O}_2\text{-Al}_2\text{O}_3$ system. The expressions for U_T , U_W , U_{dep} have been derived and discussed in ref. 20, but we here briefly recall them for the convenience of the reader

$$U_T = U_{\alpha\beta\gamma}(P) + U_W + U_{dep} - V_T \frac{C_D}{C_0} \sum_{i=1}^{n_D} P_i - \frac{C_S V_T^2}{2} n_D \quad (6)$$

where

$$U_{\alpha\beta\gamma}(P) = \sum_{i=1}^{n_D} (\alpha_i P_i^2 + \beta_i P_i^4 + \gamma_i P_i^6) \quad (7a)$$

$$U_{dep} = \frac{1}{2} \sum_{j,h=1}^{n_D} \frac{P_j P_h}{C_{j,h}} \quad (7b)$$

$$U_W = \sum_{j=1}^{n_D} \left[\frac{t_F}{2d} \sum_n \frac{k}{w} (P_j - P_n)^2 \right] \quad (7c)$$

with all symbols already defined after eqn (2) and in Fig. 1.

Fig. 5(a) reports U_T , U_{dep} and U_W versus the coupling constant k and, for each k , the energies are evaluated numerically at the point along the charge versus $E_{F,AV}$ trajectories where the charge Q is zero (see, for example, the vertical blue arrow in Fig. 2(a)–(c)); the right y-plot illustrates the corresponding μ_{2P} value.

Here it should be remarked that, due to the quasi-static operation, the energy contributions in Fig. 5(a) essentially

correspond to a minimum of U_T at the corresponding external bias V_T .

Fig. 5(a) shows that, in the considered condition at $Q \approx 0$, for low k values below approximately $2 \times 10^{-11} \text{ m}^3 \text{ F}^{-1}$ the domain wall energy U_W is much smaller than U_{dep} . For such k values the U_T is minimized through a strongly inhomogeneous polarization across the capacitor, that is illustrated in Fig. 5(b) and corresponds to large μ_{2P} values. In fact polarization pattern given by approximately $P_i \approx \pm P_r$ corresponds to a minimum of $U_{\alpha\beta\gamma}$ and to a relatively small value of the depolarization energy U_{dep} . The corresponding charge versus field characteristic is hysteretic, as illustrated in Fig. 2(c).

For increasing k values the inhomogeneous polarization in Fig. 5(b) implies a progressively larger domain wall energy U_W , so that for k values above approximately $10^{-10} \text{ m}^3 \text{ F}^{-1}$ the minimization of U_T requires a reduction of the polarization inhomogeneity and of μ_{2P} as it can be seen in Fig. 5(a). For even larger k values the penalty in terms of U_W of the inhomogeneous polarization becomes so large that the U_T minimization is found in the homogeneous polarization condition given by $P_i \approx 0$, which in fact corresponds to a minimum of both U_W and U_{dep} . The corresponding charge versus field characteristic is non hysteretic, as illustrated for example in Fig. 2(a).

Before concluding the analysis of the quasi static behavior, we here acknowledge that in this paper we neglect the possible influence of interface traps at the ferroelectric–dielectric interface, and of border or bulk traps in the dielectrics. In truly quasi static conditions the influence of trapping can be relevant,⁴¹ and some of these authors have already shown that, in the presence of interface traps, the polarization trajectories tend to deviate from the ‘S’-shaped P versus E_F curve, and that the homogeneous NC stability condition is also influenced by traps.²⁰ In this respect, the results in Fig. 2–4 correspond to quasi static conditions as far as the ferroelectric dynamics is concerned (*i.e.* the external bias V_T is very slow compared to τ_p), but the influence of traps is not explicitly addressed in this paper, and we refer the interested reader to our previous work in ref. 20.

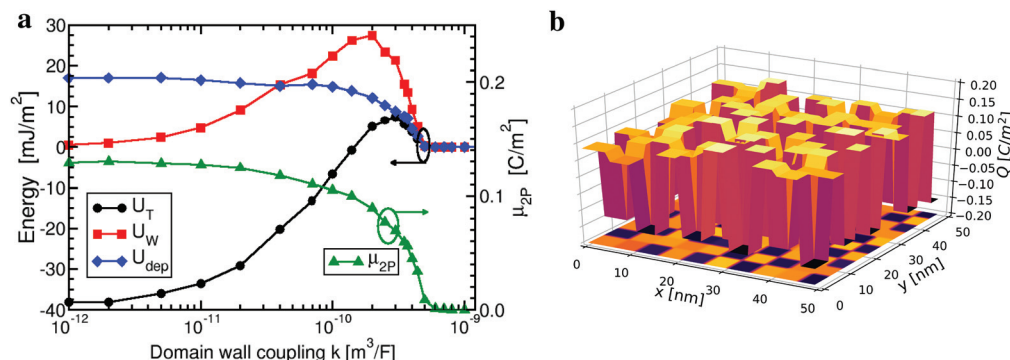


Fig. 5 Analysis of the free energy contributions. (a) Total free energy, U_T , depolarization energy, U_{dep} , and domain wall energy, U_W , versus the coupling constant k (left y-axis), and corresponding μ_{2p} value (right y-axis). For each k value, the energies and μ_{2p} are evaluated at the zero charge point (i.e. $Q \approx 0$) marked by the blue vertical arrows in Fig. 2(a)–(c). (b) Three dimensional plot for the polarization reported in a sub-region (for clarity purposes) of the MFIM structure analyzed in Fig. 2. The results correspond to the approximately zero charge point marked by the blue vertical arrow in Fig. 2(c), and to a domain wall energy coupling constant $k = 2 \times 10^{-11}$ [m³ F⁻¹].

3.3 Homogeneous NC stability condition

The results of the previous sections show that, for a quasi static operation, there exists a tight link between the fulfillment of the homogeneous NC stability condition in eqn (4) and the obtainment of polarization trajectories that track the ‘S’-shaped P versus E_F curve with a negligible hysteresis. For the Hf_{0.5}Zr_{0.5}O₂ based MFIM structures, however, such a quasi static NC behavior requires a domain wall coupling constant k larger than approximately 7×10^{-10} [m³ F⁻¹].

A k value in the range of 10^{-9} [m³ F⁻¹] appears too large, in fact much smaller k values have been reported for perovskite ferroelectrics. Ahluwalia *et al.* reported $k = 1.38 \times 10^{-11}$ m³ F⁻¹ for BaTiO₃,³⁹ and Park and co-workers have recently shown that, according to their LGD formalism and with $k = 1.38 \times 10^{-11}$ m³ F⁻¹, a homogeneous NC stability is obtained in a BaTiO₃ based MFIM structure for a ferroelectric thickness below approximately 7 nm.³ For PbTiO₃ Hoffmann and co-workers have extracted $k = 4.55 \times 10^{-11}$ m³ F⁻¹ in the ESI of ref. 19. Moreover, although to our best knowledge no attempts have been reported to extract a k value for Hf_{0.5}Zr_{0.5}O₂ from experiments, very recent first principle calculations suggest that in HfO₂ the domain wall energy should be small,⁴² resulting in small values of the coupling constant.

In order to further analyze the role of the coupling constant k we compared our findings with recent investigations also based on the LGD equations. Fig. 6(a) shows the regions in the t_F , k plane where the Hf_{0.5}Zr_{0.5}O₂–Ta₂O₅ MFIM system analyzed in Fig. 2(a)–(c) fulfills the homogeneous NC stability condition in eqn (4) for a domain size $d = 5$ nm or 3 nm. As it can be seen our results are in fairly good agreement with the semi-empirical eqn (15) in ref. 19.¶ The modest discrepancy between our results and the stability condition in ref. 19 is not unexpected. In fact the analysis in ref. 19 was carried out for a

one-dimensional periodic system and by inspecting the free energy landscapes, whereas in our model we account for a two dimensional array of domains and study the NC stabilization by using the ferroelectric dynamic equations.²⁰

Fig. 6(b) considers the BaTiO₃ based MFIM structure also analyzed in ref. 3; the material parameters can be found in Table 1.¶ The regions in the t_F , k plane fulfilling eqn (4) are shown for $d = 5$ nm and 3 nm. As it can be seen for $k = 1.38 \times 10^{-11}$ m³ F⁻¹ our simulations predict that the system can fulfill the homogeneous NC stability condition for t_F below approximately 7 nm. These findings are consistent with the t_F related analysis in ref. 3, and the inset shows that the domain polarizations at zero external bias are also consistent with ref. 3.

Fig. 6 shows that a substantially larger k value is necessary for the Hf_{0.5}Zr_{0.5}O₂ compared to the BaTiO₃ system in order to fulfill eqn (4). We verified that this is mainly due to the much larger $|\alpha|$ value of Hf_{0.5}Zr_{0.5}O₂, which is in turn related to a large difference in the coercive field.

3.4 Transient NC operation

The simulation results in section 3.1 show that the observation of a quasi static NC behavior requires the fulfillment of the homogeneous NC stability condition in eqn (4), which in turn results in unrealistically large values of the domain wall coupling constant for the Hf_{0.5}Zr_{0.5}O₂ based MFIM structures. Quite interestingly the authors themselves of ref. 37 describe their experiments as an evidence of transient NC operation.

This is consistent with the fact that authors could not observe a capacitance enhancement effect (i.e. total capacitance larger than C_D) in small-signal impedance measurements. In other words, there is no direct experimental evidence that the MFIM capacitors used in ref. 37 fulfill a homogeneous NC stability condition. Therefore we reconsidered the

¶ The condition given by eqn (15) in ref. 19 is independent of d and it assumes a t_D much larger than d , which is in fact the case in the results of Fig. 6(a) for $d = 5$ nm or 3 nm and $t_D = 13.5$ nm.

¶ Our simulations considered a MFIM structure with a dielectric thickness $t_D = 7$ nm, which is the overall dielectric thickness (3.5 nm for the upper and lower interfacial layer) employed in the MFIM structure analyzed in ref. 3.

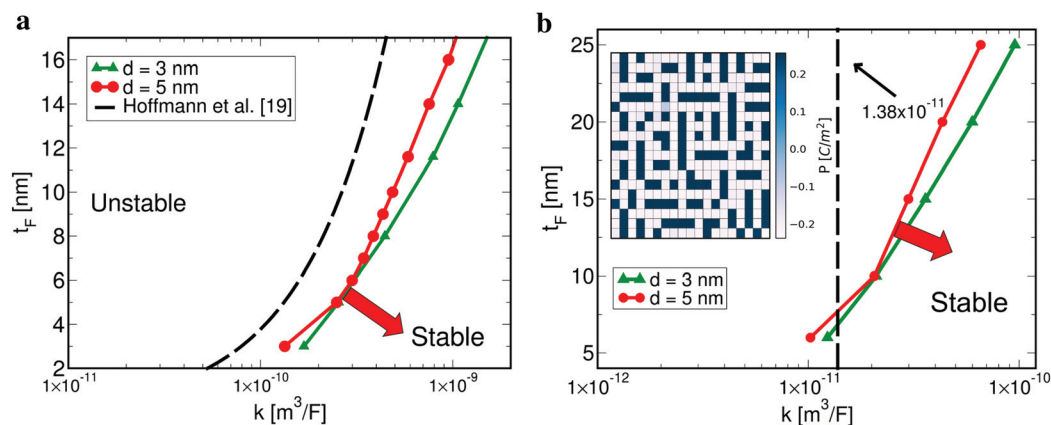


Fig. 6 Regions in the t_F , k plane fulfilling the homogeneous NC stability condition. Eqn (4) is satisfied for k values at the right of the curves reported in the figure. (a) Same $\text{Hf}_{0.5}\text{Zr}_{0.5}\text{O}_2$ – Ta_2O_5 MFIM structure as in Fig. 2(a)–(c), hence for a dielectric thickness $t_D = 13.5$ nm. The curve obtained from the semi-empirical eqn (15) in ref. 19 (dashed black line) is also shown for comparison. (b) BaTiO_3 based MFIM structure investigated in ref. 3 for a dielectric thickness $t_D = 7$ nm. The analysis in ref. 3 employed a domain wall coupling constant $k = 1.38 \times 10^{-11} \text{ m}^3 \text{ F}^{-1}$.³⁹ The inset shows the pattern of the domain polarizations calculated with our model at zero external bias and for $t_F = 10$ nm, $d = 5$ nm and $k = 1.38 \times 10^{-11} \text{ m}^3 \text{ F}^{-1}$.

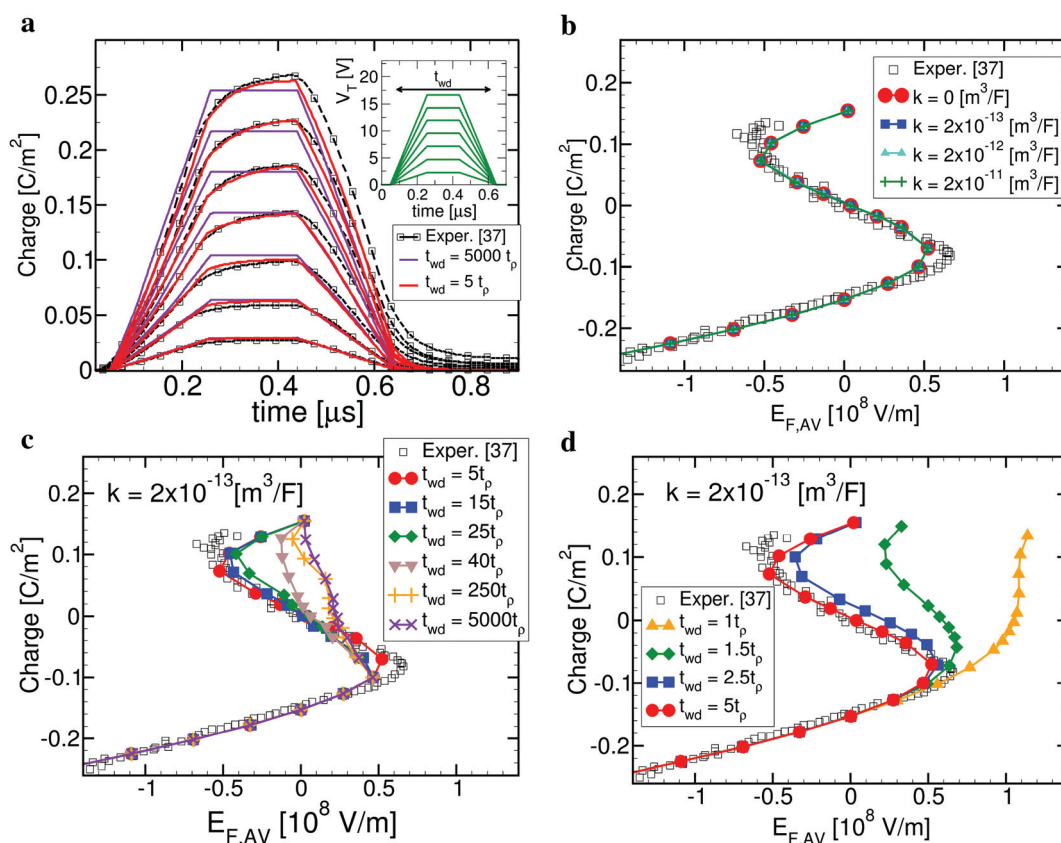


Fig. 7 Simulations for a transient NC operation. Same $\text{Hf}_{0.5}\text{Zr}_{0.5}\text{O}_2$ – Ta_2O_5 MFIM structure that has been analyzed under quasi static conditions in Fig. 2(a)–(c). Consistently with experiments,³⁷ simulations were obtained for trapezoidal V_T waveforms (see the inset in (a)), and results are illustrated for different ratios t_{wd}/t_p . For $t_{wd} = 5000t_p$ simulation results are identical to the quasi static results reported in section 3.1. (a) Simulated charge versus time waveforms for $t_{wd} = 5t_p$ or for the quasi static condition $t_{wd} = 5000t_p$; the corresponding experimental data sets are also shown.³⁷ (b) Charge versus ferroelectric field curve for $t_{wd} = 5t_p$ and for different values of the domain wall coupling constant k . (c) Same as in (b) but for progressively larger ratios t_{wd}/t_p eventually resulting in the quasi static operation. (d) Same as in (b) but for progressively smaller ratios t_{wd}/t_p .

interpretation of the experiments from a transient NC perspective.

Consistently with the experiments, we employed trapezoidal V_T waveforms that are sketched in the inset of Fig. 7(a), where t_{wd} denotes the pulse width. As already mentioned, in the ferroelectric dynamics described by eqn (2) the time scale is set by $t_p = \rho/(2|\langle\alpha\rangle|)$, so that simulation results depend on t_{wd} only through the ratio t_{wd}/t_p . Fig. 7(a) illustrates the experimental and simulated charge *versus* time waveforms for different V_T amplitudes. Simulation results are reported for either a small t_p , corresponding to the quasi static condition explored in section 3.1, or for $t_{wd}/t_p = 5$. As it can be seen the quasi static simulations do not reproduce well the experimental charge waveform, whereas for $t_{wd}/t_p = 5$ the agreement between simulations and experiments is markedly better.

The charge waveforms in Fig. 7(a) show unambiguously that experiments do not correspond to a quasi static operation. We have systematically investigated this aspect and Fig. 7(b) reports once again the charge *versus* ferroelectric field curves (as in Fig. 2), obtained from the charge waveforms corresponding to $t_{wd}/t_p = 5$. More precisely the charge reported in Fig. 7(b)–(d) is the maximum charge, approximately corresponding to the charge at end of the high V_T level. Such an evaluation of the charge in simulations emulates exactly the experimental procedure.** Quite interestingly we see that for $t_{wd}/t_p = 5$ the simulations are in good agreement with experiments and, moreover, they are essentially insensitive to the coupling constant k . In effect the simulations track the ‘S’-shaped P *versus* E_F curve and are hysteresis free even for $k \approx 0$.

Fig. 7(c) and (d) report the charge *versus* field curves obtained for different values of the ratio t_{wd}/t_p ranging from the quasi static operation (*i.e.* t_{wd}/t_p larger than about 100), down to short pulses such that the spontaneous polarization cannot respond to the external bias (*i.e.* t_{wd}/t_p smaller than about 2). As it can be seen for a t_{wd}/t_p value in the range between approximately 2.5 and 25 the simulated results can track the experiments quite closely. Fig. 7(c) shows that for slower V_T waveforms, instead, simulations approach the quasi static operation described in section 3.1. Whereas for t_{wd} values below approximately $2t_p$ the charge *versus* field curves in Fig. 7(d) deviate from the ‘S’-shaped P *versus* E_F curve; this occurs because the switching of the spontaneous polarization cannot follow the external bias, which is a behavior already reported in ref. 3.

The results in Fig. 7 suggest that the $\text{Hf}_{0.5}\text{Zr}_{0.5}\text{O}_2\text{-Ta}_2\text{O}_5$ MFIM structure can exhibit a transient NC behavior even for

negligible k values, provided that the pulse width of the external bias is between about $2.5t_p$ and $25t_p$. For a pulse width of approximately $0.5\text{ }\mu\text{s}$ (see Fig. 3 of ref. 37 and the inset of Fig. 7(a)), such an interpretation of the experiments requires that t_p be in a range between approximately 20 ns and 200 ns, which in turn leads to a resistivity ρ of the polarization switching between about 18 and 180 Ohm m. Such an estimate of ρ is consistent with the values recently reported for HZO based capacitors.^{43,44}

4 Conclusions

In this paper we have analyzed several HZO based MFIM structures and discussed the link between the macroscopic features of the MFIM operation (*e.g.* the hysteresis and the slope of the NC branches), and the corresponding microscopic picture (*e.g.* μ_{2P}). This investigation has been carried out in the framework of a comparison between our simulations and the NC measurements in ref. 37.

Our results based on the multi-domain LGD equations show that the observation of a quasi static NC behavior requires the fulfillment of the homogeneous NC stability condition in eqn (4) and that, moreover, for the $\text{Hf}_{0.5}\text{Zr}_{0.5}\text{O}_2$ based MFIM structures explored in this work this leads to unrealistically large values of the domain wall coupling constant k .

However a systematic comparison between simulations and experiments demonstrates that an MFIM system not fulfilling eqn (4) can still exhibit a transient NC behavior that closely tracks the ‘S’-shaped P *versus* E_F curve and with a very small hysteresis. In this scenario the influence of the coupling constant k on the device operation becomes weak, in fact our simulations can reproduce the experiments in ref. 37 even for $k \approx 0$.

We conclude by noting that the derivation of steady state NC stability conditions, such as eqn (4), is useful because it provides guidelines to identify material and design parameters suitable for the NC operation. However we have seen that MFIM systems that do not meet such conditions can still display a robust transient NC behavior and ‘S’-shaped P *versus* E_F characteristics. From a technological standpoint such a transient NC operation is very relevant, even because ferroelectric transients may be very fast.⁴¹

Conflicts of interest

There are no conflicts to declare.

Acknowledgements

Authors would like to thank Daniel Lizzit for useful discussions, and Michael Hoffmann for sharing some of the experimental datasets generated in ref. 37, as well as for insightful

**The evaluation of the charge in simulations corresponds to the Q_{max} of the experiments. Then in experiments the charge Q_{rev} that is reversibly stored and released in the capacitor is evaluated by subtracting from Q_{max} the charge Q_{res} , which is in turn the residual charge on the capacitor after the applied voltage goes back to zero.³⁷ Because in simulations Q_{res} is zero, our evaluation of the charge is consistent with experiments. The Q_{res} observed in experiments is ascribed to a possible charge trapping in the oxide stack, and Fig. 3(g) of ref. 37 shows that Q_{res} is in any case very small compared to Q_{max} for the experiments that we are here comparing to.

discussions. Authors are also grateful to anonymous reviewers for pointing out recent references and stimulating additional analyses that significantly improved the quality of the paper.

References

- 1 M. A. Alam, M. Si and P. D. Ye, A critical review of recent progress on negative capacitance field-effect transistors, *Appl. Phys. Lett.*, 2019, **114**, 090401, DOI: 10.1063/1.5092684.
- 2 J. Íñiguez, P. Zubko, I. Luk'yanchuk and A. Cano, Ferroelectric negative capacitance, *Nat. Mater.*, 2019, **4**, 243–256.
- 3 H. W. Park, J. Roh, Y. B. Lee and C. S. Hwang, Modeling of Negative Capacitance in Ferroelectric Thin Films, *Adv. Mater.*, 2019, **31**, 1805266, DOI: 10.1002/adma.201805266.
- 4 S. Salahuddin and S. Datta, Use of Negative Capacitance to Provide Voltage Amplification for Low Power Nanoscale Devices, *Nano Lett.*, 2008, **8**(2), 405–410, DOI: 10.1021/nl071804g.
- 5 A. C. Seabaugh and Q. Zhang, Low-Voltage Tunnel Transistors for Beyond CMOS Logic, *Proc. IEEE*, 2010, **98**(12), 2095–2110, DOI: 10.1109/JPROC.2010.2070470.
- 6 J. C. Wong and S. Salahuddin, Negative Capacitance Transistors, *Proc. IEEE*, 2019, **107**(1), 49–62.
- 7 Z. Krivokapic, U. Rana, R. Galatage, A. Razavieh, A. Aziz, J. Liu, J. Shi, H. Kim, R. Sporer, C. Serrao, A. Busquet, P. Polakowski, J. Mülle, W. Kleemeier, A. Jacob, D. Brown, A. Knorr, R. Carter and S. Banna, GLOBALFOUNDRIES, 14 nm Ferroelectric Fin-FET Technology with Steep Subthreshold Slope for Ultra Low Power Applications, in *2017 IEEE International Electron Devices Meeting (IEDM), December 2017*, ISSN 2156-017X, pp. 357–360. DOI: DOI: 10.1109/IEDM.2017.8268393.
- 8 D. Kwon, Y. Liao, Y. Lin, J. P. Duarte, K. Chatterjee, A. J. Tan, A. K. Yadav, C. Hu, Z. Krivokapic and S. Salahuddin, Response Speed of Negative Capacitance FinFETs, in *2018 IEEE Symposium on VLSI Technology, June 2018*, ISSN 2158-9682, pp. 49–50. DOI: DOI: 10.1109/VLSIT.2018.8510626.
- 9 D. J. Frank, P. M. Solomon, C. Dubourdieu, M. M. Frank, V. Narayanan and T. N. Theis, The Quantum Metal Ferroelectric Field-Effect Transistor, *IEEE Trans. Electron Devices*, 2014, **61**(6), 2145–2153, DOI: 10.1109/TED.2016.2614432.
- 10 A. Jain and M. A. Alam, Stability Constraints Define the Minimum Subthreshold Swing of a Negative Capacitance Field-Effect Transistor, *IEEE Trans. Electron Devices*, 2014, **61**(7), 2235–2242, DOI: 10.1109/TED.2013.2286997.
- 11 K. Majumdar, S. Datta and S. P. Rao, Revisiting the Theory of Ferroelectric Negative Capacitance, *IEEE Trans. Electron Devices*, 2016, **63**(5), 2043–2049, DOI: 10.1109/TED.2013.2286997.
- 12 A. I. Khan, U. Radhakrishna, K. Chatterjee, S. Salahuddin and D. A. Antoniadis, Negative Capacitance Behavior in a Leaky Ferroelectric, *IEEE Trans. Electron Devices*, 2016, **63**(11), 4416–4422.
- 13 A. I. Khan, U. Radhakrishna, S. Salahuddin and D. Antoniadis, Work Function Engineering for Performance Improvement in Leaky Negative Capacitance FETs, *IEEE Electron Device Lett.*, 2017, **38**(9), 1335–1338, DOI: 10.1109/LED.2017.2733382.
- 14 T. Rollo and D. Esseni, Energy Minimization and Kirchhoff's Laws in Negative Capacitance Ferroelectric Capacitors and MOSFETs, *IEEE Electron Device Lett.*, 2017, **38**(6), 814–817, DOI: 10.1109/LED.2017.2691002.
- 15 T. Rollo and D. Esseni, New Design Perspective for Ferroelectric NC-FETs, *IEEE Electron Device Lett.*, 2018, **39**(4), 603–606, DOI: 10.1109/LED.2018.2795026.
- 16 T. Rollo and D. Esseni, Influence of Interface Traps on Ferroelectric NC-FETs, *IEEE Electron Device Lett.*, 2018, **39**(7), 1100–1103, DOI: 10.1109/LED.2018.2842087.
- 17 S. Pentapati, R. Perumal, S. Khandelwal, M. Hoffmann, S. K. Lim and A. I. Khan, Cross-Domain Optimization of Ferroelectric Parameters for Negative Capacitance Transistors-Part I: Constant Supply Voltage, *IEEE Trans. Electron Devices*, 2020, **67**(1), 365–370, DOI: 10.1109/TED.2013.2286997.
- 18 S. Pentapati, R. Perumal, A. I. Khan and S. K. Lim, Optimal Ferroelectric Parameters for Negative Capacitance Field-Effect Transistors Based on Full-Chip Implementations-Part II: Scaling of the Supply Voltage, *IEEE Trans. Electron Devices*, 2020, **67**(1), 371–376, DOI: 10.1109/TED.2013.2286997.
- 19 M. Hoffmann, M. Pešić, S. Slesazek, U. Schroeder and T. Mikolajick, On the stabilization of ferroelectric negative capacitance in nanoscale devices, *Nanoscale*, 2018, **10**(23), 10891–10899, DOI: 10.1039/C8NR02752H.
- 20 T. Rollo, F. Blanchini, G. Giordano, R. Specogna and D. Esseni, Stabilization of negative capacitance in ferroelectric capacitors with and without a metal interlayer, *Nanoscale*, 2020, **12**, 6121–6129, DOI: 10.1039/c9nr09470a.
- 21 T. Rollo, F. Blanchini, G. Giordano, R. Specogna and D. Esseni, Revised analysis of negative capacitance in ferroelectric-insulator capacitors: analytical and numerical results, physical insight, comparison to experiments, in *2019 IEEE International Electron Devices Meeting (IEDM), Dec 2019*, pp. 7.2.1–7.2.4.
- 22 A. I. Khan, K. Chatterjee, B. Wang, S. Drapcho, L. You, C. Serrao, S. R. Bakaul, R. Ramesh and S. Salahuddin, Negative capacitance in a ferroelectric capacitor, *Nat. Mater. Lett.*, 2015, **14**, 182–186, DOI: 10.1038/nmat4148.
- 23 S. J. Song, Y. J. Kim, M. H. Park, Y. H. Lee, H. J. Kim, T. Moon, K. D. Kim, J.-H. Choi, Z. Chen, A. Jiang and C. S. Hwang, Alternative interpretations for decreasing voltage with increasing charge in ferroelectric capacitors, *Sci. Rep.*, 2016, **6**, 20825, DOI: 10.1038/srep20825.
- 24 Y. J. Kim, H. W. Park, S. D. Hyun, H. J. Kim, K. D. Kim, Y. H. Lee, T. Moon, Y. B. Lee, M. H. Park and C. S. Hwang, Voltage Drop in a Ferroelectric Single Layer Capacitor by

- Retarded Domain Nucleation, *Nano Lett.*, 2017, **17**(7), 7796–7802.
- 25 A. I. Khan, D. Bhowmik, P. Yu, S. J. Kim, X. Pan, R. Ramesh and S. Salahuddin, Experimental evidence of ferroelectric negative capacitance in nanoscale heterostructures, *Appl. Phys. Lett.*, 2011, **99**(11), 113501, DOI: 10.1063/1.3634072.
 - 26 D. J. R. Appleby, N. K. Ponon, K. S. K. Kwa, B. Zou, P. K. Petrov, T. Wang, N. M. Alford and A. O'Neill, Experimental Observation of Negative Capacitance in Ferroelectrics at Room Temperature, *Nano Lett.*, 2014, **14**(7), 3864–3868, DOI: 10.1021/nl5017255.
 - 27 P. Zubko, J. C. Wojdeł, M. Hadjimichael, S. Fernandez-Pena, A. Sené, I. Luk'yanchuk, J.-M. Triscone and J. Íñiguez, Negative capacitance in multidomain ferroelectric superlattices, *Nature*, 2016, **534**, 524–528, DOI: 10.1038/nature17659.
 - 28 T. S. Börscke, J. Müller, D. Bräuhäus, U. Schröder and U. Böttger, Ferroelectricity in hafnium oxide: CMOS compatible ferroelectric field effect transistors, in *2011 International Electron Devices Meeting, Dec 2011*, ISSN 2156-017X, pp. 24.5.1–24.5.4. DOI: DOI: 10.1109/IEDM.2011.6131606.
 - 29 D. Zhou, Y. Guan, M. Vopson, J. Xu, H. Liang, F. Cao, X. Dong and J. Mueller, Electric field and temperature scaling of polarization reversal in silicon doped hafnium oxide ferroelectric thin films, *Acta Mater.*, 2015, **99**, 240–246.
 - 30 K. S. Li, P. G. Chen, T. Y. Lai, C. H. Lin, C. C. Cheng, C. C. Chen, Y. J. Wei, Y. F. Hou, M. H. Liao, M. H. Lee, M. C. Chen, J. M. Sheih, W. K. Yeh, F. L. Yang, S. Salahuddin and C. Hu, Sub-60mV-swing negative-capacitance FinFET without hysteresis, in *2015 IEEE International Electron Devices Meeting (IEDM), Dec 2015*, pp. 22.6.1–22.6.4.
 - 31 M. H. Lee, S. T. Fan, C. H. Tang, P. G. Chen, Y. C. Chou, H. H. Chen, J. Y. Kuo, M. J. Xie, S. N. Liu, M. H. Liao, C. A. Jong, K. S. Li, M. C. Chen and C. W. Liu, Physical thickness 1.x nm ferroelectric HfZrOx negative capacitance FETs, in *2016 IEEE International Electron Devices Meeting (IEDM), Dec 2016*, pp. 12.1.1–12.1.4. DOI: DOI: 10.1109/IEDM.2016.7838400.
 - 32 P. Sharma, K. Tapily, A. K. Saha, J. Zhang, A. Shaughnessy, A. Aziz, G. L. Snider, S. Gupta, R. D. Clark and S. Datta, Impact of total and partial dipole switching on the switching slope of gate-last negative capacitance FETs with ferroelectric hafnium zirconium oxide gate stack, in *2017 Symposium on VLSI Technology, June 2017*, pp. T154–T155. DOI: DOI: 10.23919/VLSIT.2017.7998160.
 - 33 J. Van Houdt and P. Roussel, Physical Model for the Steep Subthreshold Slope in Ferroelectric FETs, *IEEE Electron Device Lett.*, 2018, **39**(6), 877–880, DOI: 10.1109/LED.2018.2829604.
 - 34 X. Li and A. Toriumi, Direct relationship between sub-60 mV/dec subthreshold swing and internal potential instability in MOSFET externally connected to ferroelectric capacitor, in *2018 IEEE International Electron Devices Meeting (IEDM), Dec 2018*, ISSN 2156-017X, pp. 31.3.1–31.3.4.
 - 35 H. Wang, M. Yang, Q. Huang, K. Zhu, Y. Zhao, Z. Liang, C. Chen, Z. Wang, Y. Zhong, X. Zhang and R. Huang, New Insights into the Physical Origin of Negative Capacitance and Hysteresis in NCFETs, in *2018 IEEE International Electron Devices Meeting (IEDM), Dec 2018*, ISSN 2156-017X, pp. 31.1.1–31.1.4. DOI: DOI: 10.1109/IEDM.2018.8614504.
 - 36 M. Hoffmann, B. Max, T. Mittmann, U. Schroeder, S. Slesazek and T. Mikolajick, Demonstration of High-speed Hysteresis-free Negative Capacitance in Ferroelectric Hf_{0.5}Zr_{0.5}O₂, in *2018 IEEE International Electron Devices Meeting (IEDM), Dec 2018*, ISSN 2156-017X, pp. 31.6.1–31.6.4. DOI: DOI: 10.1109/IEDM.2018.8614677.
 - 37 M. Hoffmann, F. P. G. Fengler, M. Herzig, T. Mittmann, B. Max, U. Schroeder, R. Negrea, P. Lucian, S. Slesazek and T. Mikolajick, Unveiling the double-well energy landscape in a ferroelectric layer, *Nature*, 2019, **565**(7740), 464–467, DOI: 10.1038/s41586-018-0854-z.
 - 38 A. K. Yadav, K. X. Nguyen, Z. Hong, P. García-Fernández, P. Aguado-Puente, C. T. Nelson, S. Das, B. Prasad, D. Kwon, S. Cheema, A. I. Khan¹, C. Hu, J. Íñiguez, J. Junquera, L.-Q. Chen, D. A. Muller, R. Ramesh and S. Salahuddin, Spatially resolved steady-state negative capacitance, *Nature*, 2019, **565**, 468–471, DOI: 10.1038/s41586-018-0855-y.
 - 39 R. Ahluwalia and D. J. Srolovitz, Size effects in ferroelectric thin films: 180° domains and polarization relaxation, *Phys. Rev. B: Condens. Matter Mater. Phys.*, 2007, **76**, 174121, DOI: 10.1103/PhysRevB.76.174121. Available: <https://link.aps.org/doi/10.1103/PhysRevB.76.174121>.
 - 40 C. H. Woo and Y. Zheng, Depolarization in modeling nanoscale ferroelectrics using the Landau free energy functional, *Appl. Phys. A*, 2008, 59–63, DOI: 10.1007/s00339-007-4355-4.
 - 41 Y. J. Kim, H. Yamada, T. Moon, Y. J. Kwon, C. H. An, H. J. Kim, K. D. Kim, Y. H. Lee, S. D. Hyun, M. H. Park and C. S. Hwang, Time-Dependent Negative Capacitance Effects in Al₂O₃/BaTiO₃ Bilayers, *Nano Lett.*, 2016, **16**(7), 4375–4381, DOI: 10.1021/acs.nanolett.6b01480.
 - 42 H.-J. Lee, M. Lee, K. Lee, J. Jo, H. Yang, Y. Kim, S. C. Chae, U. Waghmare and J. H. Lee, Scale-free ferroelectricity induced by flat phonon bands in HfO₂, *Science*, 2020, **369**(6509), 1343–1347, DOI: 10.1126/science.aba0067.
 - 43 M. Kobayashi, N. Ueyama, K. Jang and T. Hiramoto, Experimental Study on Polarization-Limited Operation Speed of Negative Capacitance FET with Ferroelectric HfO₂, in *2016 IEEE International Electron Devices Meeting (IEDM), Dec 2016*, pp. 314–317.
 - 44 J. A. T. Kim and D. A. Antoniadis, Dynamics of HfZrO₂ Ferroelectric Structures: Experiments and Models, in *2020 IEEE International Electron Devices Meeting (IEDM), Dec 2020*, pp. 441–444.